Artificial-Neural-Network-Assisted Distributed Directional Optical Fiber Torsion Sensor With the SSAF-Based Sagnac Interferometer

Jiaqi Cao, Biao Wang, Bingsen Huang, Shuqin Lou , Zhufeng Sheng, and Paul K. Chu, *Fellow, IEEE*

Abstract—A distributed optical fiber torsion sensor assisted by an artificial neural network (ANN) is designed based on the single stress-applying fiber (SSAF)-based Sagnac interferometer and demonstrated experimentally. A theoretical model is established to describe the piecewise torsion of the high birefringent fiber in the Sagnac loop, and the ANN algorithm is employed to demodulate the distributed torsion signals. The experimental results demonstrate the ability to simultaneously measure the torsion position and torsion angle when only one position along the fiber is subjected to torsion. The average R^2 and MAE of three predictions of the single torsion position are 0.984 and 0.55 cm, and those of the torsion angle are 0.998 and 1.98° for torsion angles from -120° to +120°. When two positions along the fiber are subjected to torsion, the R^2 and MAE of the torsion angle are 0.96/11.31° and 0.99/2.17° for torsion angles between -120° and +120°. The sensing system is demonstrated to demodulate the torsion of the wrist joint and elbow joint of the human arm. This promising strategy not only achieves the highest torsion position resolution and shortest response time, but also can be used to perform distributed torsion measurement and torsion direction recognition at the same time in addition to measuring the torsion at multiple positions, thereby showing great potential in applications such as robotic arms.

Index Terms—Artificial neural network (ANN) algorithm, distributed torsion sensor, sagnac interferometer.

I. INTRODUCTION

DISTRIBUTED torsion sensing is used in various fields, such as structural health monitoring, aerospace engineering, and medical applications, by providing the capability of monitoring the torsion angle at multiple positions along the structure [1], [2]. Particularly within the field of robotic arms, employed in areas like minimally invasive procedures and machining processes, accurate detection of distributed torsion is crucial to enhance both the precision and dependability of these advanced systems [3], [4], [5]. Because optical fibers have the capabilities of information transmission and sensing, optical fiber sensors can be used for torsion measurements at arbitrary positions. In addition, there are advantages such as immunity to electromagnetic interference, compact size, and exceptional corrosion resistance [6], [7], [8], boding well for distributed torsion measurements for robotic arms.

Although optical fiber torsion sensors for single-position torsion measurements have been widely investigated [9], [10], [11], there have been few reports about optical fiber distributed torsion sensing. Researchers have primarily focused on quasi-distributed torsion sensors, but torsion measurements can only be conducted at some specific locations. For instance, R. Ramalingam et al. [12] have arranged the Fiber Bragg Grating (FBG) on a parallel plate to measure the torsional stress of the plate for the quasi-distributed torsional measurement within a torsion angle range of 30°. V. Budinski et al. [13] have employed a series of in-line fiber polarizers with integrated semi-mirrors to modulate the optical power transmission by altering the polarization direction through torsion. The system consists of nine sensing segments for the measurement of torsion angles in the range of 0° - 90° with an angle resolution as low as 0.3°. However, in order to achieve more precise posture perception, it is insufficient to solely conduct torsion measurement at specific positions. Hence, it is necessary to conduct torsion angle measurements at arbitrary positions.

Researchers have recently used the backscattering technology for this purpose. G. Yin et al. [14] have designed a distributed torsion sensor using helical multi-core fibers and optical frequency domain reflectometry (OFDR) on a 1.2 m long-spanning fiber. This device shows a linear sensitivity at 1.9 pm/(rad/m) and position-aware resolution is 9.4 mm. C. Chen et al. [15] have proposed a distributed torsion sensor based on the spiral fiber utilizing frequency scanning phase-sensitive optical time-domain Reflectometry (φ-OTDR) to accomplish a measurement resolution of 1 m for a 136 m long fiber. When the device is used to measure torsion, each measurement requires approximately l to 2 minutes. The backscattering technology is

Jiaqi Cao, Biao Wang, and Shuqin Lou are with the Key Laboratory of Communication and Information Systems, Beijing Municipal Commission of Education, School of Electronic and Information Engineering, Beijing Jiaotong University, Beijing 100044, China (e-mail: 21111039@bjtu.edu.cn; b.wang@bjtu.edu.cn; shqlou@bjtu.edu.cn).

Bingsen Huang is with the School of Physical Science and Engineering, Beijing Jiaotong University, Beijing 100044, China (e-mail: 19118012@bjtu.edu.cn).

Zhufeng Sheng is with the China Center for Information Industry Development Beijing 100044, China (e-mail: shengzhufeng@ccidthinktank.com).

Paul K. Chu is with the Department of Physics, Department of Materials Science & Engineering, and Department of Biomedical Engineering, City University of Hong Kong, Hong Kong (e-mail: paul.chu@cityu.edu.hk).

capable of measuring distributed torsion angles in a relatively long range such as tens of kilometers. However, most such applications involve robotic arm posture sensing and shape reconstruction, consequently requiring high spatial resolution and real-time operation. The resolution of distributed optical fiber sensing based on backscattering is often constrained by the type of fibers and signal processing methods, thus limiting wider use. Moreover, the real-time performance of distributed measurements based on backscattering technology needs to be improved. In this respect, interferometer-based sensors may overcome these challenges. The interferometer-based sensor features a straightforward system architecture and signal processing process to offer good real-time performance. In the field of robotic arms, interferometric systems for distributed measurements have recently gained more interest [16], [17]. In particular, Sagnac interferometer-based sensors provide the advantages of stable signal transmission and anti-interference [18], [19]. Therefore, a Sagnac interferometer-based sensing system can improve the sensing properties of distributed torsion sensors.

There has been significant advance pertaining to the application of machine learning to distributed fiber sensing [20], [21], [6]. P. Hernández et al. [22] have demonstrated that deep learning models trained with real seismic data can effectively detect earthquakes by using optical fiber distributed acoustic sensors (DAS). L. Yang et al. [23] have proposed a fully connected neural network with dense and residual connections to mitigate various complex noises in real DAS data. C Karapanagiotis et al. [24] have separated the temperature information from the response of a distributed fiber optic humidity sensor using simple machine learning to resolve the temperature cross crosstalk. These studies demonstrate that machine learning plays an important role in solving problems related to spectral information extraction, spectral noise suppression, and multi-parameter identification of distributed sensors [25]. In addition, machine learning can be combined with interferometric sensing systems to not only realize distributed measurements of torsion angles, but also improve the position measurement resolution and real-time performance.

Here, we design and demonstrate experimentally a single stress-applying fiber (SSAF)-based Sagnac interferometer assisted by an artificial neural network (ANN) algorithm for distributed torsion measurements for the first time. When only one position along the SSAF is subjected to torsion, both the torsion position and torsion angle can be measured. The measurement of torsion angles when multiple positions are under torsion is validated on both the experimental platform and the human arm. This promising technique not only achieves the highest torsion position resolution (0.55 cm) and shortest response time (0.008 s), but also can be used to conduct torsion angle measurements at any position for torsion direction recognition as well as simultaneous measurement of torsion at multiple positions. Therefore, it has myriad potential applications in the field of robotic arms.

II. SENSOR STRUCTURE AND PRINCIPLE

The distributed directional optical fiber torsion sensor consists of a Sagnac interferometer in which a segment of SSAF is
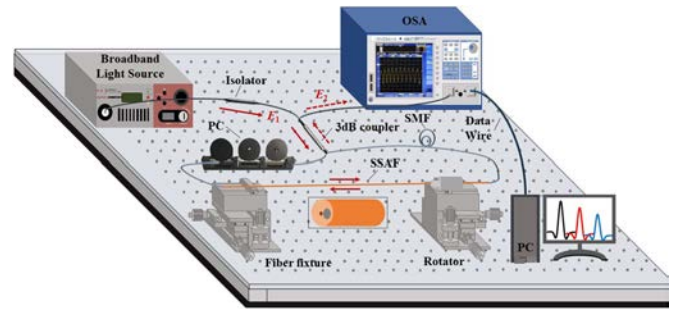

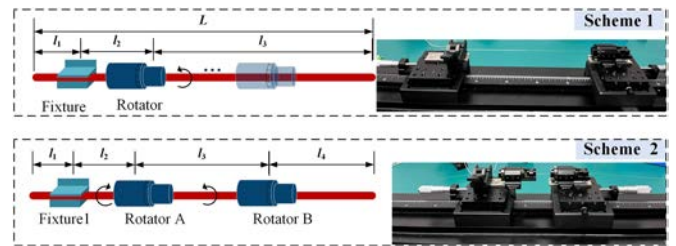Fig. 1.   Experimental setup of the distributed directional fiber optic torsion sensor.

Fig. 2.   Diagram of the torsion schemes.

fixed or adjusted with a fixed fixture or moveable rotators. A polarization controller (PC) is used to adjust the polarized state of the transmission light, and a 3-dB coupler equally divides the incident light beam into two beams, as shown in Fig. 1. A broadband light source (BBS with a wavelength range of 480 nm - 2200 nm (model SC-5-FC, YSL) is connected to the input of the 3 dB coupler through an isolator. The light E_1 from the BBS is injected into the Sagnac loop through the isolator and 3 dB coupler and then split equally into two light beams. One beam passes through the Sagnac loop in the clockwise direction and the other propagates along the anticlockwise direction. When the two beams converge at the 3dB coupler, interference occurs. The spectrum for the interference light E_2 is acquired by an optical spectrum analyzer (OSA, model MS9740A, Anritsu) and transmitted to a PC for analysis.

Two experimental schemes are contrived to measure the single position and multiple positions torsion, as shown in Fig. 2. In Scheme 1, by aiming at identifying the torsion at a single position, the SSAF is placed between one fixed fixture and one rotator. In Scheme 2, in order to identify the torsion at multiple positions, the SSAF is held by one fixed fixture and two rotators. The rotators can be moved along the rail. In order to prevent breaking at the splice points during the torsion process, both the fixed fixture and rotators are placed on the segment of SSAF away from two spice points.

When the torsion angle is changed by twisting the rotator at different positions along the SSAF, different spectral responses are produced due to the different torsion position and torsion angle. Therefore, both the torsion angle and torsion position can be demodulated in terms of the spectra responses. The torsion on the SSAF induces changes in both the polarization direction and cumulative phase difference of the transmitted polarized light, which can be described by the Jones matrix. The alteration in the polarization direction of the transmission polarized light can

be expressed by the Jones matrix:

$$R(\theta) = \begin{pmatrix} \cos\theta & \sin\theta \\ -\sin\theta & \cos\theta \end{pmatrix} \quad (1)$$

where θ is the torsion angle. The cumulative phase difference of polarized light transmission in SSAF can be expressed by:

$$J(B, L) = \begin{pmatrix} e^{-j\pi BL/\lambda} & 0 \\ 0 & e^{j\pi BL/\lambda} \end{pmatrix} \quad (2)$$

where L is the length of fiber, B is the birefringence of SSAF, and λ is the optical wavelength. When the rotator is moved to different positions of the SSAF and torsion is applied by twisting the rotator in the experiment, the sensing system can be conceptualized as dividing the SSAF into multiple cascaded sections. As shown in Scheme 1, it can be envisioned as three cascaded SSAF sections: Section I spanning from fusion point 1 to a fixed fixture with a length of l_1, Section II spanning from the fixed fixture to a rotator with a length of l_2, and Section III from the rotator to fusion point 2 with a length of l_3. When the torsion angle at the rotator is altered, only Section II experiences significant torsional stress, while Sections I and III remain virtually untwisted due to the free state. Therefore, the transmission matrices of the Sagnac loop in the clockwise direction (CW) Mcw and counterclockwise direction (CCW) Mccw can be expressed as:

$$\begin{cases} M_{cw} = R(\theta_2)J(B_0, l_3)J(B_1, l_2)R(\Delta\theta)J(B_0, l_1)R(\theta_1) \\ M_{ccw} = R(-\theta_1)J(B_0, l_1)R(-\Delta\theta)J(B_1, l_2) \\ \quad\quad \times J(B_0, l_3)R(-\theta_2) \end{cases}$$

$$(3)$$

where $R(\theta 1)$, $R(\theta 2)$, and $R(\Delta\theta)$ are the Jones matrixes of PC, fusion points, and torsion, respectively, $J(B_0, l_1)$, and $J(B_0, l_3)$ are the Jones matrixes of Sections I and III, respectively, and $J(B_1, l_2)$ is the Jones matrixe of Section II with a birefringence B_1 that is composed of both the intrinsic birefringence and torsion-induced birefringence.

As shown in Scheme 2, it can be conceptualized as four cascaded sections of SSAF. When the torsion angles of both rotators A and B are adjusted, Sections II and III undergo torsion, while Sections I and IV experience negligible torsional effects due to the free state. The transmission matrix for the clockwise direction (M_{cw}) and counterclockwise direction (M_{ccw}) in the Sagnac loop can be expressed as:

$$\begin{cases} M_{cw} = R(\theta_2)J(B_0, l_4)J(B_3, l_3)R(\Delta\theta_2) \\ \quad J(B_2, l_2)R(\Delta\theta_1)J(B_0, l_1)R(\theta_1) \\ M_{ccw} = R(-\theta_1)J(B_0, l_1)R(-\Delta\theta_1)J(B_2, l_2) \\ \quad R(-\Delta\theta_2)J(B_3, l_3)J(B_0, l_4)R(-\theta_2) \end{cases}$$

$$(4)$$

where $R(\theta_1)$ and $R(\theta_2)$ are the Jones matrices of PC and fusion points, respectively, $R(\Delta\theta_1)$ and $R(\Delta\theta_2)$ are the Jones matrices of the torsion on Sections II and III, $J(B_0, l_1)$, and $J(B_0, l_4)$ are the Jones matrices of Sections I and IV, $J(B_1, l_2)$ and $J(B_2, l_3)$ are Jones matrices of Sections II and III, and B_2 and B_3 are the birefringence under torsion for Sections II and III, respectively. According to the transmission matrices in the Sagnac loop analyzed above, the transmitted light field E_2
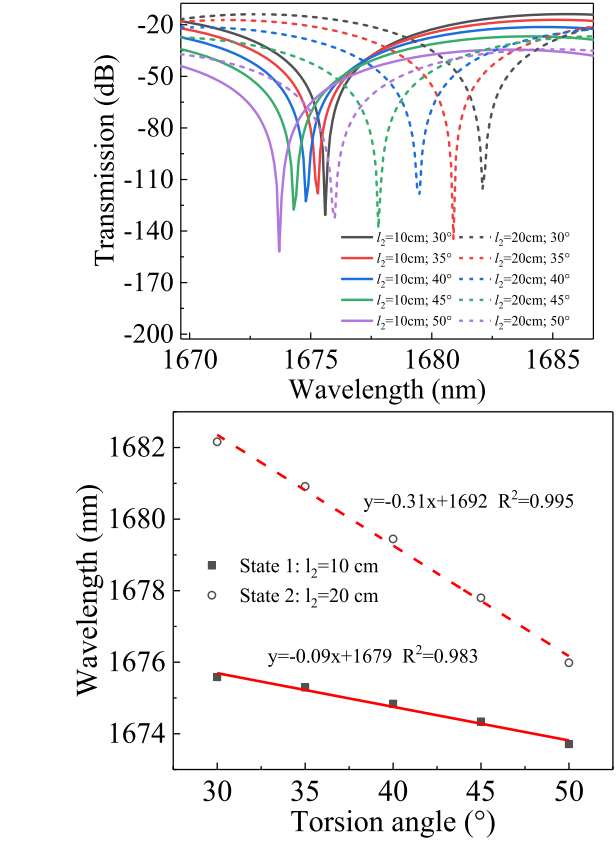

Fig. 3. (a) Simulated spectra for different torsion angles and (b) dip wavelengths for different torsion angles in the two states.

can be expressed as:

$$E_2 = (M_{cw} - M_{ccw})E_1/2. \quad (5)$$

Therefore, transmission can be expressed as:

$$T = (M_{cw} - M_{ccw})^2/4. \quad (6)$$

Based on the aforementioned theory, the transmission spectra of different torsion angles at different torsion positions are calculated based on Scheme 1. θ_1 and θ_2 are 30°, the inherent birefringence B_0 of SSAF is 2.5×10^{-4}, l_1 is 1 cm, and $\Delta\theta$ ranges from 10° to 50° in increments of 10°. The movement of the torsion position causes simultaneous changes in l_2 and l_3. To simulate this process, two states are defined in the analysis. In state 1, l_2 and l_3 are 10 cm and 44 cm, respectively and in state 2, l_2 and l_3 are 20 cm and 34 cm, respectively. Compared to state 1, state 2 corresponds to a 10 cm shift of the rotator along the direction away from the fixed fixture.

The spectra of the two states are calculated. Fig. 3 depicts transmission spectra and dip wavelengths as the torsion angles are changed from 30° to 50° for both states. Fig. 3(b) shows that the dip in the transmission spectra shifts toward shorter wavelengths with increasing torsion angles in both states 1 and 2. The torsion angle sensitivity is -0.09 nm/° and -0.31 nm/° of state 1 and state 2, respectively. Therefore, the sensitivity of the torsion angle is different when the twisting is performed at different positions. In theory, the torsion position can be demodulated by the difference in the torsion sensitivity.
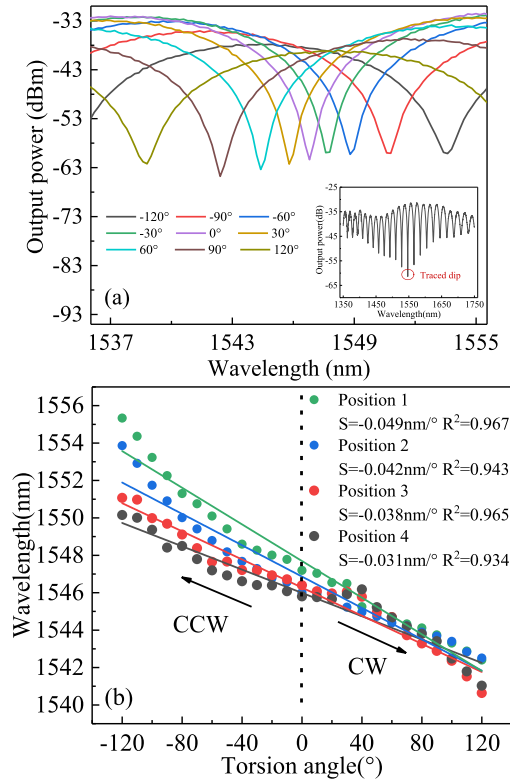
Fig. 4. (a) Experimental spectra for different torsion angles and (b) dip wavelength changes with torsion angles at different torsion positions.

Experiments are performed to verify the distributed torsion sensing performance of the system. Considering the use distributed torsion sensing by robotic arms, the length of the SSAF is 55 cm. The fixed fixture is positioned on the SSAF 2 cm from the fusion point 1. The rotator is adjusted from 18 cm to 21 cm away from the fixed fixture by steps with increments of 1 cm, thus producing four positions. At each position, the spectra of torsion angles from -120° to 120° are acquired by steps of 10°. The torsion angle in the clockwise direction is positive but negative in the counterclockwise direction. The experimental spectra for different torsion angles at a single torsion position at a distance of 21 cm away from the fixed fixture are shown in Fig. 4(a). The dip at an initial wavelength of 1546 nm is selected for tracking, and the variations of the dip wavelengths with torsion angles for different torsion positions are presented in Fig. 4(b). The dip wavelengths shift toward shorter wavelengths when the torsion direction is clockwise but to longer wavelengths when the torsion direction is counterclockwise. Therefore, the sensor can discern the torsion direction. The sensitivity of the torsion response at the four positions are analyzed. Fig. 4(b) shows the variations of the dip wavelengths with torsion angles at different torsion positions. Linear fitting reveals that R2 is 0.967 because of the nonlinear torsion characteristic [26], indicating that linear fitting is not accurate enough. There is a small difference in the torsion sensitivity for different torsion positions, and the maximum torsion sensitivity difference at the four torsion positions is only 0.018 nm/°. Considering these two factors, large errors may be

generated by the dip tracking method to demodulate the torsion position and torsion angle simultaneously.

III. DISTRIBUTED TORSION ANGLE DEMODULATED BY ANN

A. ANN Algorithm

The artificial neural network (ANN) algorithm is a computational model that emulates the functions of the nervous system, enabling it to perform various intricate learning processes [6]. Here, the ANN algorithm is employed to demodulate the torsion position and angle simultaneously. Fig. 5 overviews the demodulation process utilizing the ANN algorithm. This process includes three main steps: data acquisition and pre-processing, ANN model training and testing, as well as prediction and evaluation.

The first step involves data acquisition and pre-processing of the spectral response, as shown by the red dotted line box in Fig. 5. Initially, dataset 1 and dataset 2 are established for Scheme 1 and Scheme2, respectively. Dataset 1 is set up by capturing the spectral responses of torsion at twenty positions. The position of the rotator is adjusted from 2 cm to 21 cm away from the fixed fixture by a step of 1 cm. At each position, the spectra of torsion angles are acquired from -120° to 120° in steps of 5°. Each spectrum serves as a sample in dataset 1, resulting in a total of 980 samples. On the other hand, dataset 2 is constructed by acquiring the spectral responses of torsion at two positions. The distances between fusion point 1 and the fixed fixture are 20 cm, and the same distance of 8 cm is selected between the fixed fixture and rotator A as well as rotator A and rotator B. Rotator A undergoes torsion from -120° to 120° at a 10° interval, while at each angle for rotator A, rotator B also twists from -120° to 120° at a 10° interval. The corresponding spectra are recorded for each combination of torsion angles between rotator A and rotator B, producing a total of 625 samples in dataset 2. Each spectrum consists of 2001 output power values spanning the wavelength range from 1350 nm to 1750 nm with a resolution of 0.2 nm. These power values serve as features for each sample in both datasets. There are two labels in each dataset. In dataset 1, the labels assigned to each sample correspond to the respective torsion position and angle. In dataset 2, the labels assigned represent the corresponding torsion angles for both rotator A and rotator B. Dataset 1 corresponds to Scheme 1 shown in Fig. 2, while dataset 2 corresponds to Scheme 2. To enhance the generalization ability in each scheme, linear normalization is applied to both feature sets and label sets. Finally, the normalized dataset is divided into two subsets, in which 75% of the data are selected randomly to be the training set and the remaining 25% form the testing dataset.

The second step involves the training and testing of the ANN model as shown by the blue dotted box in Fig. 5. The samples from the training dataset are utilized to train the ANN model using the ANN algorithm. Generally, the ANN model comprises the input layer, hidden layer, and output layer. In this case, since each sample contains 2001 data points and both schemes have two labels, there are 2001 nodes in the input layer and 2 nodes in the output layer. The number of hidden layer nodes and layers is artificially determined and will be discussed later. During
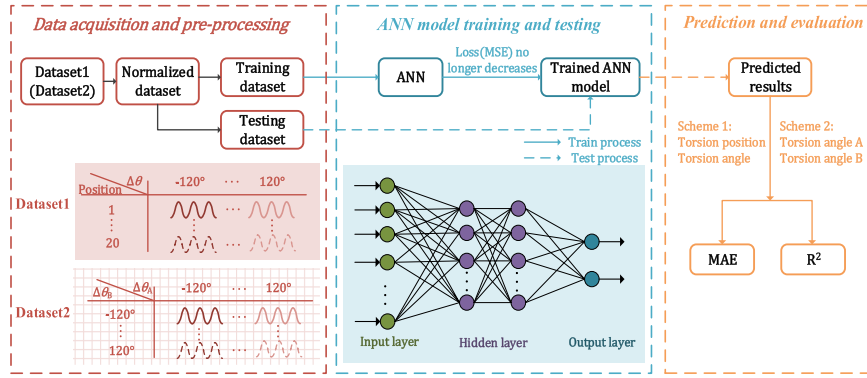
Fig. 5. Schematic diagram of the demodulated process for the distributed torsion measurement.

network training, various activation functions and weight values are applied to process the data.

In the experiment, Relu serves as the activation function. In the training process, the normalized mean square error (MSE) between the predicted values and actual values represents the loss function to evaluate the model parameters, as it captures the discrepancy the between predicted and actual values more effectively. MSE is defined in the following [27]:

$$\text{MSE} = \frac{1}{n} \sum_{i=1}^{n} (y_i - \hat{y}_i)^2, \tag{7}$$

where y_i is the average actual value, $\hat{y}_i$ is the predicted value of the ANN algorithm, and n is the number of samples. In predicting the two labels, the overall mean square error (MSE) is determined by averaging the MSE values for both labels. The model parameters (weight and bias associated with each node) are optimized by the back-propagation (BP) algorithm during multiple epochs of training to achieve minimum MSE. This minimum MSE demonstrates that the model delivers superior prediction performance for this specific parameter combination, thereby confirming successful training.

The model hyperparameters, including the number of hidden layers, nodes in each hidden layer, learning rates, and epochs, are optimized. The evaluation standard is set as the minimum MSE achieved during the training process. Fig. 6 illustrates the minimum MSE of ANN model for different hyper-parameter settings. Fig. 6(a) shows the training minimum value of MSE when there are 1, 2, 3, and 4 hidden layers for a learning rate of 0.00001 and epochs of 3000. Additionally, for each fixed number of hidden layers mentioned above, the number of nodes in each hidden layer varies as follows: 100, 300, 500, 700, and 900. It can be observed that increasing from one to two hidden layers decreases the minimum value of MSE, but further increase in the number of hidden layers does not significantly reduce in minimum MSE anymore. Hence, it is determined that two hidden layers yield the optimal characteristics. Furthermore, when the number of hidden layers is fixed, the minimum MSE value decreases gradually with the number of hidden layer nodes. The decreasing rate of MSE slows when the number of hidden layer nodes is greater than 500. However, more nodes lead to a longer
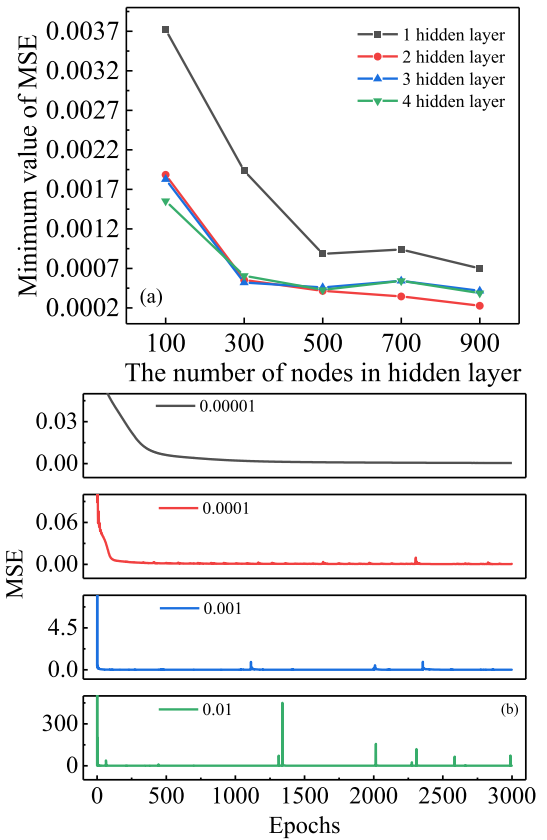

Fig. 6. Minimum value of MSE of ANN model for different numbers of hidden layers and nodes in the hidden layer(a) and MSE of different learning rates and epochs(b).

training time and therefore, the number of nodes per layer is selected to be 500.

Fig. 6(b) shows the change of MSE with different learning rates of 0.01, 0.001, 0.0001, and 0.00001 for two hidden layers in which each layer contains 500 nodes. The model is trained for a total of 3000 epochs. The MSE decreases gradually as the number of epochs increases until it reaches the minimum. A higher learning rate facilitates faster decent toward the minimum MSE, thereby reducing the required number of training epochs. However, a bigger learning rate also results in stronger oscillations of MSE during the training process. Notably, when

the learning rate is 0.00001, the MSE remains relatively stable throughout the training iterations and hence, this value is chosen as the optimal learning rate. Since it takes 3000 training epochs to reach the minimum MSE, the number of epochs to be trained is 3000. It is evident that the conditions of 2 hidden layers, 500 nodes in each hidden layer, learning rate of 0.00001, and 3000 epochs exhibit the best training effect. Consequently, this hyperparameter combination is selected for the trained optimal ANN model to predict the outcome.

The third step is to predict and evaluate the torsion position and torsion angle, as shown by the yellow dotted line box in Fig. 5. The R^2 coefficient and the mean absolute error (MAE) are used to evaluate the accuracy of the predicted values versus actual values. Specifically, R^2 as an indicator of the prediction accuracy for our model is defined as follows:

$$R^2 = 1 - \frac{\sum_i (y_i - \hat{y}_i)^2}{\sum_i (y_i - \bar{y})^2}, \tag{8}$$

where $\bar{y}$ is the average of the actual values. The closer R^2 approaches 1, the more accurate the ANN model is. To represent the prediction error more intuitively, the mean absolute error (MAE) is also introduced as expressed below:

$$MAE = \frac{1}{n} \sum_{i=1}^{n} |\hat{y}_i - y_i| \tag{9}$$

B. Single Position Torsion Demodulation

Dataset 1 is employed to train and test the ANN model to predict the torsion position and torsion angle of the single position torsion. To assess the generalization ability of the ANN model, dataset 1 is split randomly into a training dataset and testing dataset three times, and the resulting training and testing datasets are used to train and test the ANN model, respectively. The corresponding predicted results are denoted as Random0, Random1, and Random2. Fig. 7(a) and (b) present the scatter plots illustrating the predicted values of the torsion position and torsion angle versus the true values. Ideally, these data points should align perfectly along the y = x curve (indicated by the solid line) in both figures. R^2 and MAE for the torsion position are 0.984/0.56 cm, 0.985/0.53 cm, and 0.984/0.55 cm and those for the torsion angle are 0.9987/1.79°, 0.9979/1.98°, and 0.9973/2.17° for the three random splitting method of dataset 1, respectively. For the prediction results of the three times splitting dataset, the average R^2 and MAE of the torsion position prediction is 0.984/0.55 cm and that of the torsion angle prediction is 0.998/1.98°. Therefore, the ANN model can accurately predict the torsion position and torsion angle of single position torsion. Additionally, the maximum difference of the predicted MAE of the torsion position is 0.03 cm, and the maximum difference of the predicted MAE of the torsion angle is 0.38°, which demonstrate that the ANN model has good generalization ability.

The effects of the position sampling interval on the prediction accuracy are investigated. By increasing the position sampling intervals to 2 cm and 3 cm, two new datasets are constructed by recording the spectral responses in the torsion angle range
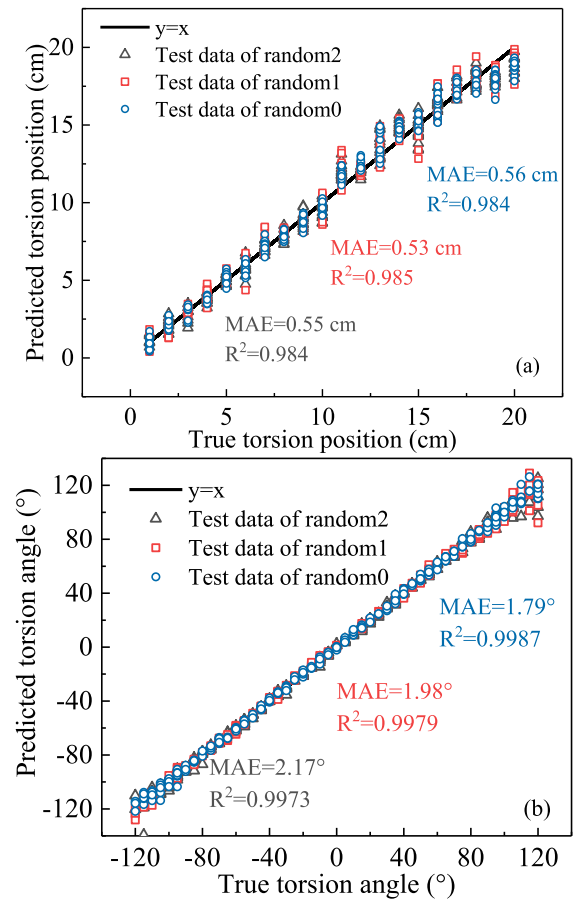

Fig. 7. Predicted torsion positions with respect to the true torsion positions (a) and predicted torsion angles with respect to the true torsion angle (b).

from -120° to 120° at an interval of 5° for each torsion position. Therefore, the datasets with the position sampling intervals of 1 cm, 2 cm, and 3 cm contain 980, 490, and 343 samples, respectively. These datasets are utilized to train the ANN models to predict both the torsion position and torsion angle. The predicted results are summarized in Table I which shows that the variation in the position sampling interval has minimal impact on the prediction accuracy of the torsion position and angle. Specifically, when the position sampling intervals are 1 cm, 2 cm, and 3 cm, the maximum difference in MAE for the torsion position predictions is only 0.09 cm. Similarly, concerning the torsion angle prediction, the maximum difference in MAE is merely 0.21°. Therefore, it is possible to increase the position sampling interval without compromising the prediction accuracy, thereby reducing the workload required for the dataset establishment.

The impact of the angle sampling interval on the prediction accuracy is analyzed. Two new datasets are constructed with a position sampling interval of 1 cm and angle sampling intervals of 10° and 20°, respectively. The torsion angle measurement range is kept between -120° and 120°. Therefore, the datasets for angle sampling intervals of 5°, 10°, and 20° contain 980, 500, and 260 samples, respectively. These datasets are then utilized to train ANN models to predict the torsion position and torsion angle as shown in Table II. According to Table II, the prediction accuracy of the torsion angle decreases gradually with increasing

TABLE I
PREDICTED RESULTS FOR DIFFERENT SAMPLING INTERVALS OF TORSION POSITIONS

Position sampling interval	Torsion position		Torsion angle	
	MAE	R^2	MAE	R^2
1cm	0.56	0.984	1.79°	0.9987
2cm	0.47	0.986	1.68°	0.9984
3cm	0.48	0.986	1.89°	0.9985

TABLE II
PREDICTED RESULTS FOR DIFFERENT SAMPLING INTERVALS OF TORSION ANGLES

Angle sampling interval	Torsion position		Torsion angle	
	MAE	R^2	MAE	R^2
5°	0.56	0.984	1.79°	0.9987
10°	0.68	0.973	2.58°	0.993
20°	0.62	0.974	3.34°	0.969

angle sampling intervals, but the increase in the angle sampling interval has only a small effect on the prediction accuracy of the torsion position. Therefore, a decrease of the angle sampling interval in the dataset can improve the torsion angle prediction resolution of the ANN models.

The subsequent investigation focuses on the prediction accuracy of the different measurement regions on the SSAF. The position near the fixed fixture is referred to as the near end, while the position far away the fixed fixture is labeled as the distal end. To ensure comprehensive training of the ANN model, the dataset is created by packaging the spectral data of 15 torsion positions with a position sampling interval of 1 cm. For comparison, six datasets are constructed using spectral data from positions 1 to 15, 2 to 16, 3 to 17, 4 to 18, 5 to 19, and 6 to 20, respectively. The near-distal characteristic of each dataset is denoted as d. Correspondingly, the values for d for these six datasets are 1, 2, 3, 4, 5 and 6, respectively. The smaller the value of d, the closer it is to the fixed fixture. Fig. 8 shows the predicted results of the torsion position and torsion angle for different ds. With increasing d, the MAE of the torsion position prediction decreases gradually with R^2 being above 0.967, proving that the prediction accuracy increases gradually. However, the maximum difference between the predicted MAE of different datasets is 0.215 cm, which accounts for 1.08% of the whole measurement range (20 cm). In addition, with increasing d, R^2 and MAE of the torsion angle prediction show small fluctuations. The maximum difference between the predicted MAE of different datasets is 0.939° and R^2 is above 0.984, thus accounting for 0.39% of the entire measurement range (240°). This implies only a slight change in the prediction accuracy of the torsion position and torsion angle at the near and distal ends.

Finally, the impact of SSAF length on the distributed torsion prediction accuracy is investigated using the ANN model with a 65 cm long SSAF inserted into the Sagnac interferometer. Fig. 9(a) displays the spectra of the sensor with the 65 cm long SSAF and 55 cm long SSAF. The FSR values for the 55 cm
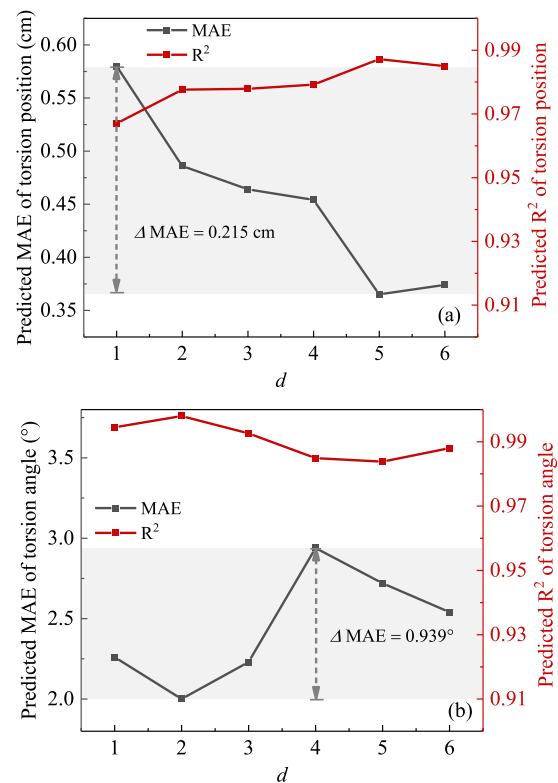

Fig. 8. Variations of the predicted (a) torsion positions and (b) torsion angle for different d.

and 65 cm long SSAF are measured to be 18.9 nm and 15.3 nm, respectively. The dataset is constructed by applying torsion to the 65 cm long SSAF in the same manner as the 55 cm long SSAF for a position sampling interval of 1 cm and angle sampling interval of 10°. Based on this dataset, the ANN model is trained for the prediction of the distributed torsion and Fig. 9 presents the predicted results revealing that R^2 and MAE of the torsion
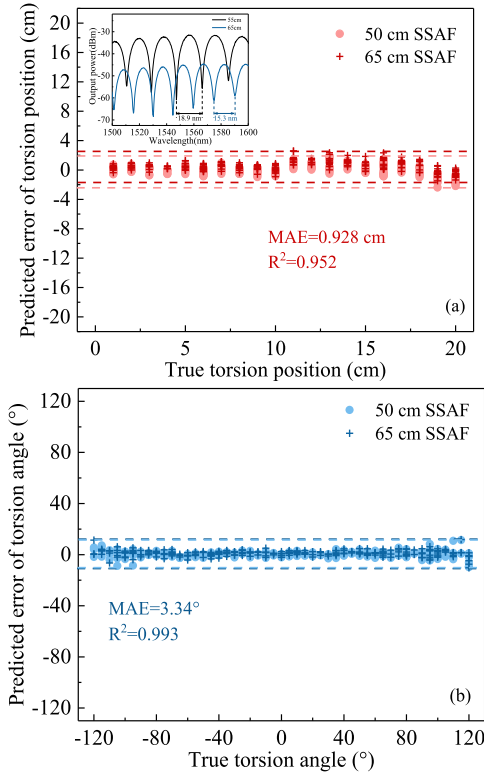
Fig. 9. Predicted torsion positions with respect to the true torsion positions (a) and predicted torsion angles with respect to the true torsion angle (b) for the 50 cm SSAF and 65 cm SSAF, respectively.
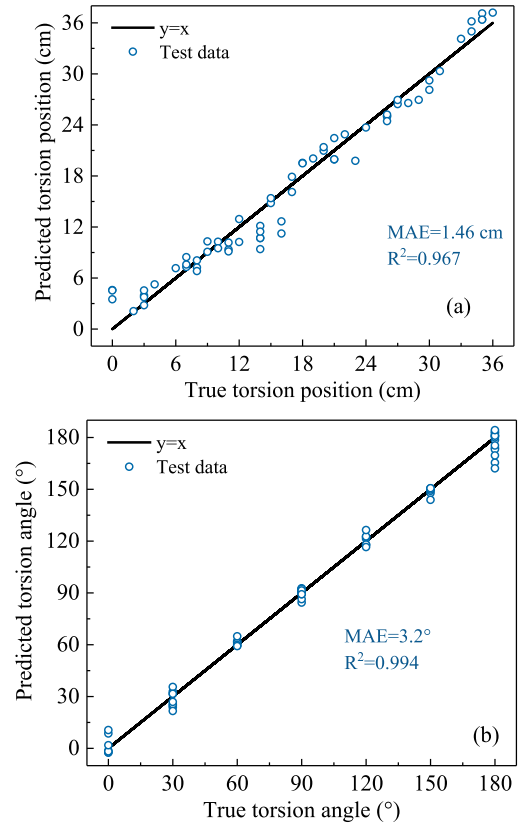

Fig. 10. Predicted torsion positions with respect to the true torsion positions (a) and predicted torsion angles with respect to the true torsion angle (b) for the panda polarization maintaining fiber, respectively.

position prediction for the sensor with the 65 cm long SSAF are 0.952 and 0.928 cm, while R^2 and MAE of the torsion angle predicted results are 0.993 and 3.34°, respectively. Compared with the predicted results of the 55 cm long SSAF, the prediction accuracy based on the dataset of the sensor with the 65 cm long SSAF decreases slightly for both torsion position and torsion angle. This can be attributed to the longer fiber lengths resulting in smaller FSR which may lead to spectral overlap in the spectral shift consequently reducing the prediction accuracy.

C. Verification Experiment of Universality

To validate the widespread applicability of our method, the experiment is carried on the Panda polarization maintaining fiber-based Sagnac interferometer. A 50 cm length of Panda polarization maintaining fiber is inserted into the Sagnac loop. For the experimental dataset, the spectral responses to torsion at thirty-six different positions are recorded by moving the rotator in 1 cm increments. At each position, the spectra of torsion angles from 0° to 180° are acquired by steps of 30°. Each captured spectrum is included as an individual sample in the dataset, amassing a total of 259 samples. The predictive performance of ANN algorithm based on the Panda polarization maintaining fiber dataset is illustrated in Fig. 10. The R^2 and MAE for the torsion position are 0.967 and 1.46 cm, and those for the torsion angle are 0.994 and 3.2°, respectively. Although the prediction accuracy of Panda polarization maintaining

fiber-based interferometer is slightly less than that of SSAF-based interferometer, it is still considered to be at a relatively high level. Moreover, the predicted accuracy can be improved by reducing the angle sampling interval and optimizing the hyperparameters of ANN model. Therefore, the ANN algorithm is proven to be adaptable to predict torsion angles and torsion position of various types of high birefringence fibers-based interferometer.

D. Multi-Position Torsion Demodulation

The ANN model is trained and tested based on dataset 2 to predict the torsion angles at multiple positions simultaneously as shown in Fig. 11. The scatter plot illustrates the alignment of the predicted values with the true values for the torsion angles at position A and position B, showing a close alignment with the y = x curve. The prediction performance for torsion angles at position A is reflected R^2 of 0.96 and MAE of 11.31°, while for torsion angles at position B, R^2 of 0.99 and MAE of 2.17° are observed. The results provide evidence that the ANN model can achieve torsion angle demodulation at multiple positions.

To demonstrate the practicality of the sensing system, the torsion angles of the wrist and elbow joint are simultaneously measured by placing the SSAF on the human arm. As shown in Fig. 12(a), the SSAF is securely affixed to the arm by tape at position A near the elbow joint and position B near the wrist joint with one end of the two rods fixed at the elbow joint and wrist

TABLE III
COMPARISON OF DISTRIBUTED TORSION SENSORS

Reference	Resolution	Time	Distributed type	Directionality	Multi-positions
[12]	--	--	Quasi-distributed	No	No
[13]	170 cm/0.3°	--	Quasi-distributed	No	No
[14]	0.94 cm/--	--	Distributed	Yes	Yes
[15]	100 cm/--	1-2min	Distributed	Yes	No
This work	0.55 cm/1.79°	0.008s	Distributed	Yes	Yes
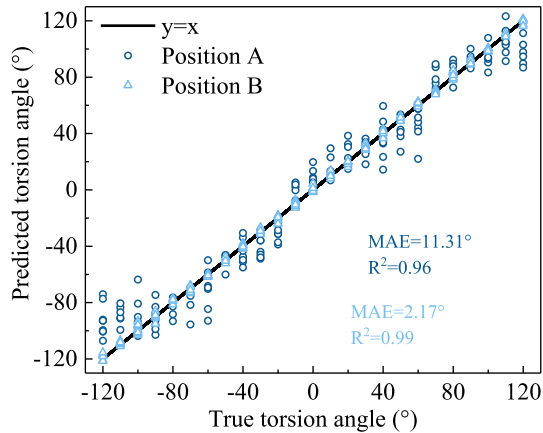
Fig. 11. Predicted torsion angles with respect to the true torsion angles at multiple positions.
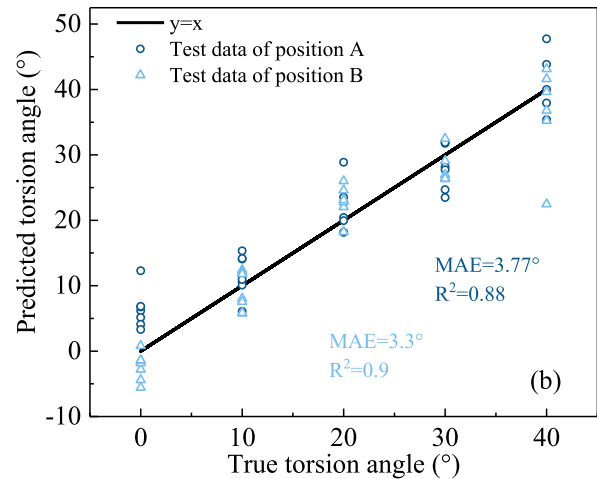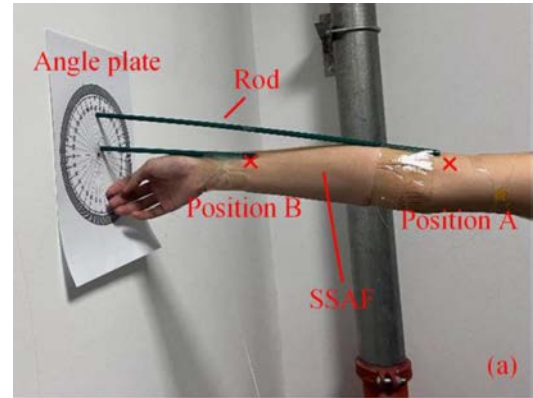
joint, respectively, while the other end of the two rods points to an angle plate adhered on the wall in order to determine torsion angles of positions A and B, respectively. The wrist joint is twisted from 0° to 40° at 10° intervals. Meanwhile, for each torsion angle of the wrist joint, the elbow joint is also twisted from 0° to 40° at a 10° interval. The dataset is constructed by collecting the spectral responses for all combination of the two torsion angles of the wrist and elbow joints. In order to increase the sample size of the dataset, the spectrum corresponding to each twist angle combination is recorded five times and a total of 125 samples are collected for the dataset. Similarly, we randomly allocate 75% (93 samples) as the training dataset and the remaining 25% (32 samples) as the testing dataset. The ANN model has two hidden layers and each hidden layer consists of 500 nodes. The learning rate is to 0.00001. Owing to the limited number of samples available in this particular dataset compared to previous datasets in our experiments, the epochs are set to be 1000. The prediction results are shown in Fig. 12(b).

The scatter plot in Fig. 12(b) shows the predicted values versus true values of the torsion angle at position A and position B. Each scatter dot is in line with the y = x curve, with R^2 value and MAE for the torsion angles at position A being 0.88 and 3.77° and position B being 0.9 and 3.3°, respectively. The results show that the sensor can indeed be used to measure the distributed torsion of the human arm. However, limited by the experimental condition, the sampling interval of the torsion angle is 10°. In future applications, higher prediction accuracy can be achieved

Fig. 12. (a) Schematic and (b) predicted results of the test of the sensing system.

by reducing the angle sampling interval making this strategy more suitable for robotic arms.

To illustrate the advantages of the system, we compare with other distributed torsion sensing systems in terms of the resolution, distribution type, and directionality, whether multiple points can be measured at the same time, and the required time. The results are listed in Table III. This ANN algorithm-assisted SSAF-based Sagnac interferometer shows a high torsion position resolution (0.55 cm) in the distributed torsion measurement. Although the torsion angle resolution is not the highest, it can be improved by reducing the angle sampling interval. In addition, compared to other distributed torsion measurement

methods such as backscattering, this method shows the shortest response time (0.008 s) thus facilitating real-time monitoring. More importantly, this method can be used for distributed torsion measurement and torsion direction recognition at the same time in addition to simultaneous measurement of the torsion at multiple positions. It thus has great application prospects in various fields such as robotic arms.

IV. CONCLUSION

The ANN assisted distributed optical fiber torsion sensor is designed based on the SSAF-based Sagnac interferometer and demonstrated experimentally. Simultaneous measurement of the torsion position and torsion angle can be achieved when only one position along the fiber is subjected to torsion. The average R^2 and MAE values of three predictions of the single torsion position are 0.984/0.55 cm and those for the torsion angle are 0.998/1.98°. The effects of the position sampling interval and angle sampling interval on the prediction accuracy of the torsion position and torsion angle are discussed. Experimental results demonstrate that the variation of the position sampling interval has minimal impact on the prediction accuracy of the torsion position and torsion angle. The variation of the angle sampling interval has a small effect on the prediction accuracy of the torsion position, and the prediction accuracy of the torsion angle decreases gradually with larger angle sampling intervals. When torsion is applied to the near and distal ends of the sensor, the prediction accuracy at the near end and distal end show only small changes. When two positions along the fiber are subjected to torsion, the R^2 and MAE values for the predicted torsion position and angle are 0.96/11.31° and 0.99/2.17°, respectively. Furthermore, the system can be deployed on the human arm to achieve simultaneous prediction of the torsion angle of the wrist joint and elbow joint. The system can measure the distributed torsion measurement and recognize the torsion direction at the same time, besides the simultaneous measurement of torsion at multiple positions. It thus has great potential in many applications such as robotic arms.

REFERENCES

[1] A. Montoya et al., "Assisted operation of a robotic arm based on stereo vision for positioning near an explosive device," *Robotics*, vol. 11, no. 5, 2022, Art. no. 100.

[2] A. Puzatova et al., "Large-scale 3D printing for construction application by means of robotic arm and gantry 3D printer: A review," *Buildings*, vol. 12, no. 11, 2022, Art. no. 2023.

[3] R. Kobayashi, H. Nabae, and K. Suzumori, "Large torsion thin artificial muscles tensegrity structure for twist manipulation," *IEEE Robot. Automat. Lett.*, vol. 8, no. 3, pp. 1207–1214, Mar. 2023.

[4] B. Xu et al., "Orthogonal single-mode helical Bragg gratings created in fiber cladding for vector bending measurement," *Opt. Lett.*, vol. 48, no. 2, pp. 452–455, 2023.

[5] B. Sun, F. Li, F. Feng, K. Wan, K. Zhou, and Z. Zhang, "Fabrication of optical stretchable curvature sensors with high linearity," *J. Lightw. Technol.*, vol. 41, no. 19, pp. 6423–6427, Oct. 2023.

[6] G. Liu et al., "Real-time monitoring and prediction method of commercial building fire temperature field based on distributed optical fiber sensor temperature measurement system," *J. Building Eng.*, vol. 70, 2023, Art. no. 106403.

[7] W. Shen et al., "Monitoring and quantification of non-uniform corrosion induced mass loss of steel piles with distributed optical fiber sensors," *Automat. Construction*, vol. 148, 2023, Art. no. 104769.

[8] H. P. Wang et al., "Parametric reflection of the quasi-distributed optical fiber sensors with flexible packaging layer for bending strain measurement," *Opt. Laser Technol.*, vol. 158, 2023, Art. no. 108893.

[9] Z. Song, Y. Li, and J. Hu, "Directional torsion sensor based on a two-core fiber with a helical structure," *Sensors*, vol. 23, no. 6, 2023, Art. no. 2874.

[10] R. Zhao, H. Liu, and X. Shu, "High-performance vector torsion sensor based on high polarization-dependent in-fiber Mach–Zehnder interferometer," *Opt. Exp.*, vol. 31, no. 5, pp. 8844–8854, 2023.

[11] Y. Zheng, J. Li, Y. Liu, Y. Li, and S. Qu, "Novel torsion sensor based on the interaction between modal interference and polarization interference," *J. Lightw. Technol.*, vol. 42, no. 7, pp. 2513–2521, Apr. 2024.

[12] R. K. Ramalingam, R. Nast, and H. Neumann, "Fiber Bragg grating sensors for distributed torsional strain measurements in a (RE) BCO tape," *IEEE Sensors J.*, vol. 15, no. 4, pp. 2023–2030, Apr. 2015.

[13] V. Budinski and D. Donlagic, "Quasi-distributed twist/torsion sensor," *Opt. Exp.*, vol. 24, no. 23, pp. 26282–26299, 2016.

[14] G. Yin et al., "Distributed directional torsion sensing based on an optical frequency domain reflectometer and a helical multicore fiber," *Opt. Exp.*, vol. 28, no. 11, pp. 16140–16150, 2020.

[15] C. Chen et al., "Distributed twist sensing using frequency-scanning φ-OTDR in a spun fiber," *Opt. Exp.*, vol. 31, no. 11, pp. 17809–17819, 2023.

[16] A. M. Biondi et al., "Pipeline structural health monitoring using distributed fiber optic sensing textile," *Opt. Fiber Technol.*, vol. 70, no. 11, 2022, Art. no. 102876.

[17] P. Zhang et al., "SNR enhancement for Brillouin distributed optical fiber sensors based on asynchronous control," *Opt. Exp.*, vol. 30, no. 3, pp. 4231–4248, 2022.

[18] Q. Chen et al., "An optical fiber sensor for the detections of liquid level and strain through cascading Sagnac interference and modal interference," *Infrared Phys. Technol.*, vol. 127, 2022, Art. no. 104387.

[19] C. Liu et al., "Sagnac interferometer-based optical fiber strain sensor with exceeding free spectral measurement range and high sensitivity," *Opt. Laser Technol.*, vol. 159, 2023, Art. no. 108935.

[20] L. Avellar et al., "Machine learning-based analysis of multiple simultaneous disturbances applied on a transmission-reflection analysis based distributed sensor using a nanoparticle-doped fiber," *Photon. Res.*, vol. 11, no. 3, pp. 364–372, 2023.

[21] Y. Liu and Y. Bao, "Automatic interpretation of strain distributions measured from distributed fiber optic sensors for crack monitoring," *Measurement*, vol. 211, 2023, Art. no. 112629.

[22] P. D. Hernández, J. A. Ramírez, and M. A. Soto, "Deep-learning-based earthquake detection for fiber-optic distributed acoustic sensing," *J. Lightw. Technol.*, vol. 40, no. 8, pp. 2639–2650, Apr. 2022.

[23] L. Yang et al., "Denoising distributed acoustic sensing data using unsupervised deep learning," *Geophysics*, vol. 88, no. 4, pp. V317–V332, 2023.

[24] C. Karapanagiotis et al., "Distributed humidity fiber-optic sensor based on BOFDA using a simple machine learning approach," *Opt. Exp.*, vol. 30, no. 8, pp. 12484–12494, 2022.

[25] A. Venketeswaran et al., "Recent advances in machine learning for fiber optic sensor applications," *Adv. Intell. Syst.*, vol. 4, no. 1, 2022, Art. no. 2100067.

[26] J. Cao et al., "High sensitivity vector torsion sensor based on a single Stress-Applying fiber Sagnac interferometer," *Opt. Fiber Technol.*, vol. 80, 2023, Art. no. 103431.

[27] B. Huang et al., "Machine-learning-assisted omnidirectional bending sensor based on a cascaded asymmetric dual-core PCF sensor," *Opt. Lett.*, vol. 48, no. 19, pp. 4929–4932, 2023.